



Heat transfer efficiency of hierarchical corrugated sandwich panels

Shanyouming Sun^{a,b,c}, Yinglong Sheng^a, Shangsheng Feng^{c,d,*}, Tian Jian Lu^{b,e,*}



^a State Key Laboratory for Strength and Vibration of Mechanical Structures, Xi'an Jiaotong University, Xi'an 710049, PR China

^b State Key Laboratory of Mechanics and Control of Mechanical Structures, Nanjing University of Aeronautics and Astronautics, Nanjing 210016, PR China

^c Bioinspired Engineering and Biomechanics Center (BEBC), Xi'an Jiaotong University, Xi'an 710049, PR China

^d The Key Laboratory of Biomedical Information Engineering of Ministry of Education, School of Life Science and Technology, Xi'an Jiaotong University, Xi'an 710049, PR China

^e MIIT Key Laboratory of Multifunctional Lightweight Materials and Structures (MLMS), Nanjing University of Aeronautics and Astronautics, Nanjing 210016, PR China

ARTICLE INFO

Keywords:

Hierarchical porous structure
Artificial intelligence optimization
Heat transfer
Sandwich panel
Thermo-mechanical design

ABSTRACT

As a kind of biomimetic materials, ultralight hierarchical porous structures possessing excellent mechanical properties such as load bearing, impact energy absorption, vibration reduction and noise attenuation have been exploited. Often, these porous structures exhibit continuous flow passages that allow for cooling fluids to pass through, thus enabling simultaneous load-bearing and active heat dissipation. This study investigated the convective cooling efficiency of a sandwich panel with hierarchical corrugated core subjected to heating from the face sheets and active cooling through the core. Built upon the classical fin approach, a theoretical model coupling wall heat conduction and fluid convection in the core was established for the hierarchical corrugated-core sandwich panel, covering the full range of fluid flow (from laminar, transition to turbulent). The theoretical model predictions were validated against full numerical simulations. Based on the theoretical model, an artificial intelligence optimization method (*i.e.*, the ant colony algorithm) was adopted to find the optimal combination of key independent geometric parameters of the sandwich panel for maximized heat transfer performance. For the problem of multi-variables optimization, it was demonstrated that the ant colony algorithm is superior in terms of computational time to the traditional exhaustive search method. For a given pressure drop, a set of optimum geometric parameters corresponding to maximum cooling efficiency was found for the proposed hierarchical corrugated-core sandwich panel.

1. Introduction

After millions of years of evolution, materials in nature have formed elegant and orderly structures with unique and excellent attributes [1]. Interestingly, although the components of these structures often have poor performance when they are taken out separately, once the components are assembled into hierarchical structures, these structures possess excellent mechanical properties macroscopically [2]. Hierarchical structures span multiple length scales to ensure that the inner microstructures of different scales could collaborate efficiently [1].

Nacre shell and biological skeleton are two typical examples of natural materials with hierarchical structures [3]. The mechanical properties of natural nacre are much higher than that of synthetic products. A highly complex microstructure is hidden behind this performance in which features are well defined and controlled on several length scales, which is the result of a bottom-up manufacturing approach.

In this method, small building blocks self-assemble, mineralize and form larger elements [2]. This transformation from low level to high level is realized through the process of hierarchical structures. Through this program, the “growth” from small scale to large scale provides great flexibility for the selection of materials, and the structure can be adjusted / optimized on different length scales according to specific functional requirements [4]. In contrast, the traditional manufacturing method is top-down, *i.e.*, the material is removed to obtain the desired shape and components. The hierarchy of bones is another typical example of the natural hierarchical structures, as shown in Fig. 1(a) [5]. At the nanoscale, self-assembled triple-helix collagen molecules and plate-shaped hydroxyapatite nanocrystals are the basic components of the hierarchical structures [2]. They form collagen fibrils through certain arrangement and combination. At the microscale, the mineralized collagen fibrils spiral with varying degrees periodically around the central axis [5] forming a cylindrical spiral structure called osteons, which becomes the basic unit of the compact

* Corresponding authors at: Bioinspired Engineering and Biomechanics Center (BEBC), Xi'an Jiaotong University, Xi'an 710049, PR China (S. Feng); State Key Laboratory of Mechanics and Control of Mechanical Structures, Nanjing University of Aeronautics and Astronautics, Nanjing 210016, PR China (T.J. Lu).

E-mail addresses: shangshengfeng@xjtu.edu.cn (S. Feng), tjlu@nuaa.edu.cn (T. Jian Lu).

<https://doi.org/10.1016/j.compstruct.2021.114195>

Received 13 February 2021; Revised 24 May 2021; Accepted 27 May 2021

Available online 29 May 2021

0263-8223/© 2021 Elsevier Ltd. All rights reserved.

Nomenclature

| | | | |
|-------------|--|-------------|--|
| a | width of large ducts | $Q_{st,1}$ | heat flux flowing along negative x at node $n + 1$ on top substrates |
| b | width of small ducts | $Q_{st,2}$ | heat flux flowing along positive x at node $n + 1$ on top substrates |
| t | thickness of vertical struts | $Q_{i,f}$ | heat transferred from vertical struts between node i to $i + 1$ to fluid in large ducts |
| r | thickness of horizontal struts | $Q_{i,mv}$ | heat dissipation from vertical strut between node i and $i + 1$ to fluid in small duct i |
| t_s | thickness of substrates | $Q_{i,mhu}$ | heat dissipation from horizontal strut at node i to fluid in small duct i |
| L | length of sandwich panels | $Q_{i,mhd}$ | heat dissipation from horizontal strut at node $i + 1$ to fluid in small duct i |
| n | number of small ducts | D | hydraulic diameter of ducts |
| q_1, q_2 | heat flux of top and bottom substrates | α | aspect ratio of ducts |
| T_c | temperature of cooling water | Nu | Nusselt number |
| Δp | pressure drop of ducts | Re | Reynolds number |
| $T_{f,i}$ | average temperature of fluid in small ducts denoted by i ($i = 1, 2, \dots, n$) | f | flow friction factor |
| $T_{f,n+1}$ | average temperature of fluid in large ducts | $T_{s,ave}$ | area weighted average temperature of solid at any xy plane in fully developed region |
| $T_{s,i}$ | temperature of node denoted by i ($i = 1, 2, \dots, n$ from bottom to top) where vertical and horizontal struts intersect | $T_{f,ave}$ | bulk temperature of fluid at the corresponding xy plane in fully developed region |
| h_f | interfacial heat transfer coefficient in large ducts | h_w | overall heat transfer coefficient of hierarchical corrugated sandwich panel |
| h_m | interfacial heat transfer coefficient in small ducts | q_{ave} | constant heat flux imposed to top and bottom substrates |
| u_f | velocity in large ducts | | |
| u_m | velocity in small ducts | | |
| $Q_{o,i}$ | outcoming heat flux from node i | | |
| $Q_{e,i}$ | incoming heat flux at node $i + 1$ | | |
| $Q_{m,i}$ | heat flux flowing to horizontal struts (from vertical struts) at node $i + 1$ | | |
| $Q_{sb,1}$ | heat flux flowing along negative x at node 1 on bottom substrates | | |
| $Q_{sb,2}$ | heat flux flowing along positive x at node 1 on bottom substrates | | |

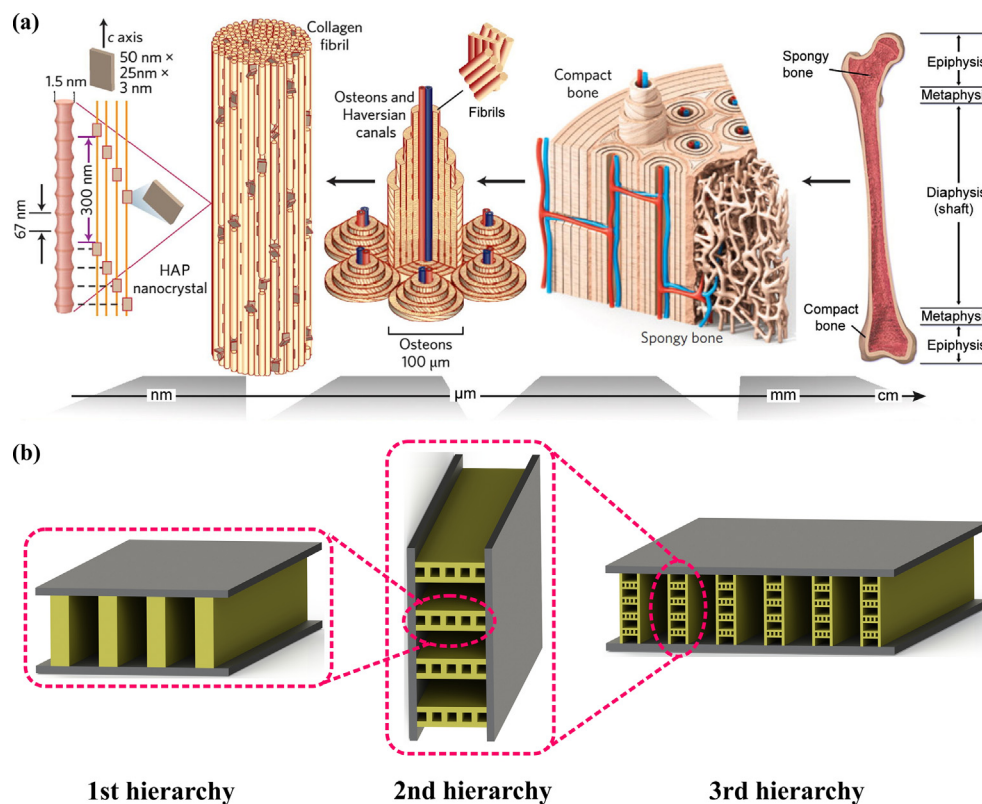


Fig. 1. Schematic illustration of biomimetic hierarchical structures. (a) Hierarchical structure of the bone: on the nanoscale, self-assembled triple-helix collagen molecules and plate-shaped hydroxyapatite nanocrystals are the basic components of the hierarchical structures [2]. They form collagen fibrils through certain arrangement and combination. At the microscale, the mineralized collagen fibrils spiral with varying degrees periodically around the central axis [5] forming a cylindrical spiral structure called osteons, which becomes the basic unit of the compact bone with Haversian canals around the blood vessels [6]. (b) Hierarchical corrugated sandwich panel considered in this study.

bone with Haversian canals around the blood vessels [6]. In essence, functions and structures are closely linked, e.g., biological structures are often determined by their functions [2]. Organisms in nature often evolve different microstructures according to different requirements such as load conditions, and their macro performance largely benefits from these hierarchical structures [1].

Although considerable progress has been made in the field of engineering structures, it is still challenging to design materials with comprehensive properties. In aerospace, power system, transportation and other major engineering fields, the main structural components often need to withstand extremely high heat flux and pressure load [7]. For example, the wall of a rocket engine combustion with a thrust-weight ratio of 10 needs to withstand 1850–1950 K high temperature and 2.5–3.0 MPa high pressure [8]. The increasingly harsh working environment puts forward higher requirements for material and structure design [9]. Inspired by the biological hierarchical structures, previous studies have introduced the concept of hierarchy into the design of traditional sandwich structures to improve the load capacity and heat dissipation of the structure [10].

The hierarchical porous structures have been extensively investigated due to the superior mechanical properties [11–17]. For example, by replacing the cell wall of regular honeycombs with the Kagome and triangular lattice, the stiffness of hierarchical honeycombs is about two orders of magnitude higher than that of the regular honeycombs [11]. Kooistra et al. [12] studied the transverse compression mechanism of hierarchical corrugated core sandwich panels and found that the second-order trusses have higher compressive and shear collapse strengths than the first-order trusses at equivalent mass. Fan et al. [13] demonstrated the effectiveness of hierarchical honeycomb structures in improving the stiffness and plastic collapse strength of thin-walled structures. Sun and Pugno [14] achieved significant in-plane stiffness improvement of hexagonal honeycomb using multifunctional hierarchical characteristics. Sun et al. [15] studied the in-plane compressive behavior of hierarchical triangular lattice structures. The results showed that the average crushing force of hierarchical triangular lattice structures is greater than that of single-cell structures and multi-cell structures. Taylor et al. [16] added hierarchy characteristics into honeycombs of graded design to avoid the reduction of Young's modulus. Tao et al. [17] prepared square hierarchical honeycombs (SHHs) using 3D printing technology and tested their in-plane compressive strength characteristics. The compressive strength of SHHs was found 79.5% higher than that of the regular square honeycombs (RSHs) under the condition of equal mass. Wu et al. first studied the failure mechanisms of hierarchical lattice materials such as corrugated-pyramidal cores [18] and pyramidal-pyramidal cores [19]. These authors demonstrated that structural hierarchy could tune the mechanical response of lattice materials and effectively increase their structural buckling resistance.

Besides the static mechanical properties, hierarchical porous structures have also shown advantages in dynamic performance such as energy absorption than traditional structures. Sun and co-authors [20,21] integrated the concept of hierarchical structure into honeycombs, and explored honeycombs with first-order and second-order hierarchy under out-of-plane load. They found that the specific energy absorption of these two different hierarchies can be increased by >80% and 180% respectively. Inspired by the microstructure of bamboo vascular bundles, Hu et al. [22] proposed a new bionic honeycomb tubular nested structure by connecting the circular tubes in hexagonal arrangement which could significantly improve the specific energy absorption performance compared to the original honeycomb. Yin et al. [23] compared three bio-inspired hierarchical honeycomb structures based on hexagonal, Kagome and triangular tessellations. They found that the energy absorption performance of triangular hierarchical honeycombs is the best amongst the three types of hierarchy, which is twice that of conventional honeycombs. Zhang et al. [10] proposed a fractal hierarchical hexagonal structure inspired by bionic

structures such as spider webs. The simulation results showed that the hierarchical structure could significantly improve the energy absorption capacity compared with the single wall non-hierarchical structure and the second-order design was the optimal at a given mass.

The existing studies have mainly focused on mechanical properties of hierarchical structures, only a few studies investigated the thermal properties. Chen et al. [24] reported that the introduction of hierarchy into regular honeycombs can improve thermal resistance and thermal anisotropy. Xu et al. [25] demonstrated an efficient thermal management network based on a hierarchical structure of one-dimensional filaments, e.g., carbon nanotubes, which could increase the overall thermal conductivity meanwhile change the temperature distribution near the heat source. However, these studies have only considered the heat conduction behavior of hierarchical structures.

In fact, convective flow transport is a critical function of natural hierarchical structures such as wood. Specifically, wood absorbs ions and water naturally during the process of metabolism. This process is completed by wood fiber composed of hollow and slender tracheid units. Pores in the fiber wall allow fluid to flow between cells. In addition, a tracheid is composed of thousands of micro cellulose, forming a multi-channel mesoporous structure, which is very suitable for absorbing and transporting water and essential ions [26]. As a biomimetic material, hierarchical porous structures have continuous flow passages which allow for fluid flow and enable convective cooling. The sandwich panel with hierarchical core is promising to be used in scenarios where simultaneous load-bearing and heat dissipation are required such as thrust chamber [27,28] and Jet Blast Deflector (JBD) [29,30]. The thermofluidic properties of sandwich panels with traditional core (lattice structure [31,32] metal foam [33,34] textile [35] honeycomb [36,37] etc.) have been well understood. However, the convective heat transfer characteristics of hierarchical sandwich panel is still elusive due to the non-homogeneous pore sizes. How to predict, characterize and optimize the convective cooling efficiency of the hierarchical porous structures is yet to be resolved.

This study aims to investigate the thermal properties of hierarchical corrugated-core sandwich panels as shown in Fig. 1(b) subjected to heating from face sheets and active cooling through the core. For convenience, we take the 2nd level hierarchical structure as an example to establish the theoretical and numerical models, although the methods can be extended to other hierarchical structures with periodic pore morphologies. In terms of active cooling, the present hierarchical corrugated-core structure resembles to the foam fins proposed for electronics cooling [38] as both having porous solids of high surface area separated by straight flow channels. However, the present hierarchical corrugated-core structure with periodic pore geometry would reduce the flow resistance and pumping power compared with the disordered metal foam [39]. On the other hand, the present hierarchical corrugated-core structure can be regarded as the 2nd level hierarchy of the traditional fin structures [40] that have been widely used in cooling industry. Noteworthy, in terms of mechanical properties, the present structure with higher order hierarchy tends to be superior [2] which is promising to be used as lightweight thermo-mechanical structure therefore.

2. Theoretical model

Fig. 2 displays the hierarchical corrugated sandwich panel of the 2nd hierarchy considered in the present study, along with definition of key geometric parameters. There are two different-sized ducts in the hierarchical structure, i.e., large ducts between two neighboring porous solids and small ducts with a unit cell of porous solid, both having rectangular shapes as depicted in Fig. 2(a). Independent geometric parameters of the considered hierarchical structure include: height of sandwich (H), length of sandwich (L), width of large ducts (a), width of small ducts (b), height of small ducts (c), number of small ducts (n),

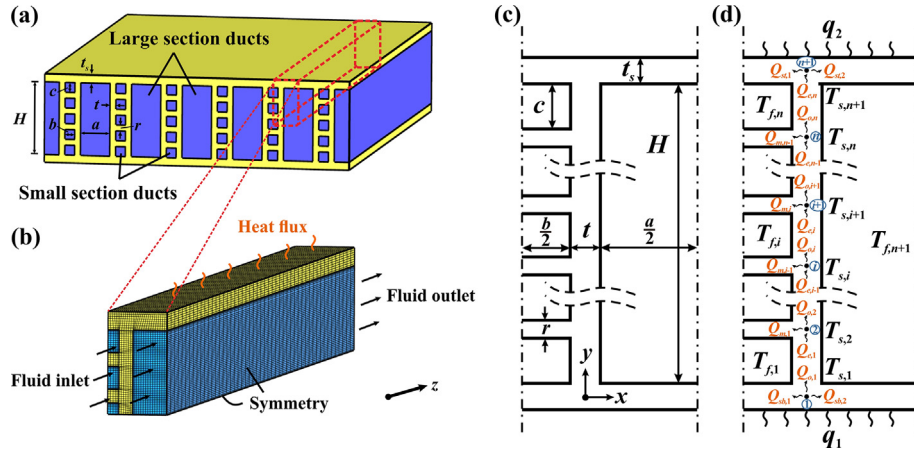


Fig. 2. Definition of problem: (a) schematic of the 2nd order hierarchy corrugated-core sandwich panel; (b) computational domain and mesh for numerical simulation of forced convection heat transfer; (c) definition of geometric parameters in a unit cell; (d) notation of thermal parameters defined for deriving the theoretical model.

thickness of vertical struts (t), thickness of horizontal struts (r), and thickness of substrates (t_s). Among them, height of small ducts (c) can be converted from the number of small ducts (n), as $c = (H - (n - 1)r) / n$. Height and length of the sandwich panel were hold constant in the study. Also, in accordance with the usual practice in convective heat transfer, substrates were used to denote the face sheets of the sandwich, with the top and bottom substrates assumed to have equal thickness.

A theoretical model based on the classical fin approach [37] was established to predict the convective heat transfer efficiency of the hierarchical corrugated sandwich. Specifically, the top and bottom substrates were heated by constant heat flux q_1 and q_2 , respectively, and the heat was taken away by a cooling fluid through the core. The cooling fluid flowed into the core at the initial temperature of T_c , and the pressure difference between the inlet and outlet was Δp across the sandwich panel of length L , as shown schematically in Fig. 2. With reference to Fig. 2(d), from bottom to top, the average temperature of the fluid in the small ducts was denoted sequentially as $T_{f,1}, T_{f,2}, \dots, T_{f,n}$. For the convenience of subsequent programming, the average temperature of the fluid in the large duct was denoted by $T_{f,n+1}$. The points where the vertical and horizontal struts intersected were denoted by node 1, node 2, ..., node $n + 1$ from bottom to top. Correspondingly, the node temperatures were denoted as $T_{s,1}, T_{s,2}, \dots, T_{s,n+1}$, with the subscript s representing the solid.

To establish the theoretical model, the following assumptions were made:

- 1) The thickness of struts was much smaller than the width of the duct, *i.e.*, one-dimensional (1-D) heat conduction in each strut was assumed.
- 2) Lateral heat conduction along flow direction was ignored.
- 3) Flow and heat transfer in the hierarchical structure was fully developed, *i.e.*, entrance/exit effects were ignored.

Based on the classical fin approach, Lu [37] established a corrugated wall model to predict the convective heat transfer efficiency of metallic honeycombs under constant temperature boundary condition. Later, Liu et al. [41] modified the Lu model [37] by considering heat transfer in horizontal struts as well. The Lu model [37] was further modified for microchannel heat sinks under constant heat flux boundary condition by considering energy balance in the substrates [40]. Nevertheless, these models all assumed uniform fluid temperature along the vertical direction (*i.e.*, perpendicular to the direction of cool-

ing flow) of sandwich panel, whereas in reality the fluid temperature in a duct adjacent the substrate should be higher than that in a duct located at the center of sandwich core. In this study, we extended Lu's corrugated wall model [37] for convection heat transfer in hierarchical corrugated sandwich panel under constant heat flux boundary condition. In the model, heat conduction both in the vertical and horizontal struts and in the substrates were coupled with heat convection of cooling fluid in each individual flow duct. Details of temperature modeling for the solids (struts and substrates) and the cooling fluid in each duct were presented below.

2.1. Temperature of struts and substrates

For fully developed flow, we considered heat conduction in solid struts and substrates only in the cross-section perpendicular to flow, *i.e.*, in the xy plane of Fig. 2(d), and modelled fluid temperature in each duct varying along the streamwise direction (*i.e.*, z direction).

2.1.1. Temperature distribution along vertical struts

Upon assuming that the temperature of node i was known, heat conduction equation and boundary conditions along the vertical struts from node i to node $i + 1$ were written as:

$$k \frac{\partial^2 T}{\partial y^2} - \frac{h_f}{t} (T - T_{f,n+1}) - \frac{h_m}{t} (T - T_{f,i}) = 0 \quad (1)$$

$$y = 0, T = T_{s,i}; y = c, T = T_{s,i+1} \quad (2)$$

where h_f and h_m are the interfacial heat transfer coefficient in the large and small ducts, respectively; k is the thermal conductivity of solid; $T_{s,i}$ is the solid temperature at node i , $T_{f,i}$ is the average temperature of fluid in the small ducts beside node i , $T_{f,n+1}$ is the average temperature of fluid in the large ducts, where $i = 1, 2, 3, \dots, n$ and n is the number of small ducts.

The solution of Eqs. (1), (2) led to temperature distribution along the vertical struts, as:

$$T = C_{i,1} e^{\lambda_1 y} + C_{i,2} e^{\lambda_2 y} + \frac{h_f T_{f,n+1} + h_m T_{f,i}}{h_f + h_m} \quad (3)$$

Then the outgoing heat flux from node i ($Q_{o,i}$) and the incoming heat flux at node $i + 1$ ($Q_{e,i}$) could be calculated:

$$Q_{o,i} = -kt \left. \frac{\partial T}{\partial y} \right|_{y=0} = -kt(C_{i,1} \lambda_1 + C_{i,2} \lambda_2) \quad (4)$$

$$Q_{e,i} = -kt \frac{\partial T}{\partial y} \Big|_{y=c} = -kt(C_{i,1}\lambda_1 e^{\lambda_1 c} + C_{i,2}\lambda_2 e^{\lambda_2 c}) \quad (5)$$

where the coefficients $C_{i,1}$, $C_{i,2}$ and the eigenvalue λ_1 , λ_2 are:

$$\lambda_1 = \sqrt{\frac{h_f + h_m}{kt}} \lambda_2 = -\sqrt{\frac{h_f + h_m}{kt}} \quad (6)$$

$$C_{i,1} = \frac{(T_{s,i} + T_{s,i+1})(h_f + h_m) - 2(T_{f,i}h_m + T_{f,n+1}h_f)}{2\left(e^{\sqrt{\frac{h_f + h_m}{kt}}} + 1\right)(h_f + h_m)} - \frac{T_{s,i} - T_{s,i+1}}{2\left(e^{\sqrt{\frac{h_f + h_m}{kt}}} - 1\right)} \quad (7)$$

$$C_{i,2} = \frac{(T_{f,n+1}h_f + T_{f,i}h_m)}{\left(e^{\sqrt{\frac{h_f + h_m}{kt}}} + 1\right)(h_f + h_m)} - \frac{e^{\sqrt{\frac{h_f + h_m}{kt}}} T_{s,i+1} - T_{s,i}}{e^{2\sqrt{\frac{h_f + h_m}{kt}}} - 1} - \frac{(T_{f,n+1} - T_{s,i})h_f + (T_{f,i} - T_{s,i})h_m}{h_f + h_m} \quad (8)$$

2.1.2. Temperature distribution along horizontal struts

Similar to the case of vertical struts, heat conduction equation and boundary conditions of the horizontal strut at node $i + 1$ could be written as:

$$k \frac{\partial^2 T}{\partial x^2} - \frac{h_m}{r} (T - T_{f,i}) - \frac{h_m}{r} (T - T_{f,i+1}) = 0 \quad (9)$$

$$x = 0, T = T_{s,i+1}; x = \frac{b}{2}, \frac{\partial T}{\partial x} = 0 \quad (10)$$

where $i = 1, 2, 3, \dots, n-1$, $T_{f,1}$ and $T_{f,n}$ represent the fluid temperature in the duct nearby the bottom and top substrates, respectively.

Solution of Eqs. (9), (10) led to temperature distribution along the horizontal strut as:

$$T = D_{i,1} e^{\zeta_1 x} + D_{i,2} e^{\zeta_2 x} + \frac{T_{f,i} + T_{f,i+1}}{2} \quad (11)$$

Then the heat flux flowing to the horizontal strut (from the vertical struts) at node $i + 1$ ($Q_{m,i}$) was:

$$Q_{m,i} = -kr \frac{\partial T}{\partial x} \Big|_{x=0} = -kr\zeta_1 (D_1 - D_2) \quad (12)$$

where the coefficients $D_{i,1}$, $D_{i,2}$ and the eigenvalue ζ_1 and ζ_2 are:

$$\zeta_1 = \sqrt{\frac{2h_m}{kr}} \quad \zeta_2 = -\sqrt{\frac{2h_m}{kr}} \quad (13)$$

$$D_{i,1} = -\frac{T_{f,i} + T_{f,i+1} - 2T_{s,i+1}}{2\left(e^{\sqrt{\frac{2h_m}{kr}}} + 1\right)} \quad (14)$$

$$D_{i,2} = -\frac{T_{f,i} + T_{f,i+1} - 2T_{s,i+1}}{2\left(e^{\sqrt{\frac{2h_m}{kr}}} + 1\right)} e^{\sqrt{\frac{2h_m}{kr}}} \quad (15)$$

2.1.3. Temperature distribution in substrates

Since both the bottom and top substrates were involved in heat transfer with fluids in small and large ducts nearby the substrates, temperature distribution of the bottom (or top) substrate would be solved separately for two sections, i.e., the left nearby small duct and the right nearby large duct.

Heat transfer in the left section of bottom substrate (contacting with fluid in the small duct) could be described as:

$$k \frac{\partial^2 T}{\partial x^2} - \frac{h_m}{t_s} (T - T_{f,1}) = 0 \quad (16)$$

$$x = 0, T = T_{s,1}; x = \frac{b}{2}, \frac{\partial T}{\partial x} = 0 \quad (17)$$

By solving Eqs. (16) and (17), we obtained temperature distribution of bottom substrate along the negative x direction, as:

$$T = E_{sb,1} e^{\eta_{b,1} x} + E_{sb,2} e^{\eta_{b,2} x} + T_{f,1} \quad (18)$$

Then the heat flux flowing along negative x at node 1 on bottom substrate ($Q_{sb,1}$) was calculated as:

$$Q_{sb,1} = -kt_s \frac{\partial T}{\partial x} \Big|_{x=0} = -kt_s \sqrt{\frac{h_m}{kt_s}} (E_{sb,1} - E_{sb,2}) \quad (19)$$

where the coefficients $E_{sb,1}$, $E_{sb,2}$ and the eigenvalue $\eta_{b,1}$, $\eta_{b,2}$ are:

$$\eta_{b,1} = \sqrt{\frac{h_m}{kt_s}} \quad \eta_{b,2} = -\sqrt{\frac{h_m}{kt_s}} \quad (20)$$

$$E_{sb,1} = \frac{1}{2} \left(\tanh\left(\frac{b}{2} \sqrt{\frac{h_m}{kt_s}}\right) - 1 \right) (T_{f,1} - T_{s,1}) \quad (21)$$

$$E_{sb,2} = -\frac{1}{2} \left(\tanh\left(\frac{b}{2} \sqrt{\frac{h_m}{kt_s}}\right) + 1 \right) (T_{f,1} - T_{s,1}) \quad (22)$$

Similarly, heat transfer in the right section of bottom substrate (contacting with fluid in the large duct) could be described as:

$$k \frac{\partial^2 T}{\partial x^2} - \frac{h_f}{t_s} (T - T_{f,n+1}) = 0 \quad (23)$$

$$x = 0, T = T_{s,1}; x = \frac{a}{2}, \frac{\partial T}{\partial x} = 0 \quad (24)$$

Temperature distribution of bottom substrate along the positive x direction was obtained as:

$$T = E_{sb,3} e^{\eta_{b,3} x} + E_{sb,4} e^{\eta_{b,4} x} + T_{f,n+1} \quad (25)$$

The heat flux flowing along positive x at node 1 on bottom substrates ($Q_{sb,2}$) was calculated as:

$$Q_{sb,2} = -kt_s \frac{\partial T}{\partial x} \Big|_{x=0} = -kt_s \sqrt{\frac{h_f}{kt_s}} (E_{sb,3} - E_{sb,4}) \quad (26)$$

where the coefficients $E_{sb,3}$, $E_{sb,4}$ and the eigenvalue $\eta_{b,3}$, $\eta_{b,4}$ are:

$$\eta_{b,3} = \sqrt{\frac{h_f}{kt_s}} \quad \eta_{b,4} = -\sqrt{\frac{h_f}{kt_s}} \quad (27)$$

$$E_{sb,3} = \frac{1}{2} \left(\tanh\left(\frac{a}{2} \sqrt{\frac{h_f}{kt_s}}\right) - 1 \right) (T_{f,n+1} - T_{s,1}) \quad (28)$$

$$E_{sb,4} = -\frac{1}{2} \left(\tanh\left(\frac{a}{2} \sqrt{\frac{h_f}{kt_s}}\right) + 1 \right) (T_{f,n+1} - T_{s,1}) \quad (29)$$

Next, heat transfer in the left section of top substrate (contacting with fluid in the small duct) was considered, governed by:

$$k \frac{\partial^2 T}{\partial x^2} - \frac{h_m}{t_s} (T - T_{f,n}) = 0 \quad (30)$$

$$x = 0, T = T_{s,n+1}; x = \frac{b}{2}, \frac{\partial T}{\partial x} = 0 \quad (31)$$

Temperature distribution of top substrate along the negative x direction was thence obtained as:

$$T = E_{st,1}e^{\eta_{t,1}x} + E_{st,2}e^{\eta_{t,2}x} + T_{f,n} \quad (32)$$

The heat flux flowing along negative x at node $n + 1$ on top substrates ($Q_{st,1}$) was:

$$Q_{st,1} = -kt_s \frac{\partial T}{\partial x} \Big|_{x=0} = -kt_s \sqrt{\frac{h_m}{kt_s}} (E_{st,1} - E_{st,2}) \quad (33)$$

where the coefficients $E_{st,1}$, $E_{st,2}$ and the eigenvalue $\eta_{t,1}$, $\eta_{t,2}$ are:

$$\eta_{t,1} = \sqrt{\frac{h_m}{kt_s}} \quad \eta_{t,2} = -\sqrt{\frac{h_m}{kt_s}} \quad (34)$$

$$E_{st,1} = \frac{1}{2} \left(\tanh \left(\frac{b}{2} \sqrt{\frac{h_m}{kt_s}} \right) - 1 \right) (T_{f,n} - T_{s,n+1}) \quad (35)$$

$$E_{st,2} = -\frac{1}{2} \left(\tanh \left(\frac{b}{2} \sqrt{\frac{h_m}{kt_s}} \right) + 1 \right) (T_{f,n} - T_{s,n+1}) \quad (36)$$

Finally, heat transfer in the right section of top substrate (contacting with fluid in the large duct) was governed by:

$$k \frac{\partial^2 T}{\partial x^2} - \frac{h_f}{t_s} (T - T_{f,n+1}) = 0 \quad (37)$$

$$x = 0, T = T_{s,n+1}; \quad x = \frac{a}{2}, \frac{\partial T}{\partial x} = 0 \quad (38)$$

Temperature distribution of top substrate along the positive x direction was obtained as:

$$T = E_{st,3}e^{\eta_{t,3}x} + E_{st,4}e^{\eta_{t,4}x} + T_{f,n+1} \quad (39)$$

from which heat flux flowing along positive x at node $n + 1$ on top substrates ($Q_{st,2}$) was calculated as:

$$Q_{st,2} = -kt_s \frac{\partial T}{\partial x} \Big|_{x=0} = -kt_s \sqrt{\frac{h_f}{kt_s}} (E_{st,3} - E_{st,4}) \quad (40)$$

where the coefficients $E_{st,3}$, $E_{st,4}$ and the eigenvalue $\eta_{t,3}$, $\eta_{t,4}$ are:

$$\eta_{t,3} = \sqrt{\frac{h_f}{kt_s}} \quad \eta_{t,4} = -\sqrt{\frac{h_f}{kt_s}} \quad (41)$$

$$E_{st,3} = \frac{1}{2} \left(\tanh \left(\frac{a}{2} \sqrt{\frac{h_f}{kt_s}} \right) - 1 \right) (T_{f,n+1} - T_{s,n+1}) \quad (42)$$

$$E_{st,4} = -\frac{1}{2} \left(\tanh \left(\frac{a}{2} \sqrt{\frac{h_f}{kt_s}} \right) + 1 \right) (T_{f,n+1} - T_{s,n+1}) \quad (43)$$

2.1.4. Heat flux equilibrium in solid region

As shown in Fig. 2(d), balance of heat flux at node $i + 1$ was established as:

$$Q_{m,i} + Q_{o,i+1} = Q_{e,i} \quad (44)$$

Substituting Eqs.(4), (5), (12) into Eq.(44) and simplifying the equation, we obtained:

$$\begin{aligned} & -\frac{kt \sqrt{\frac{h_f+h_m}{kt}}}{\sinh \left(c \sqrt{\frac{h_f+h_m}{kt}} \right)} T_{s,i} + \left(2kt \coth \left(c \sqrt{\frac{h_f+h_m}{kt}} \right) \sqrt{\frac{h_f+h_m}{kt}} + \frac{kr \left(e^{b \sqrt{\frac{2h_m}{kr}}} - 1 \right) \sqrt{\frac{2h_m}{kr}}}{e^{b \sqrt{\frac{2h_m}{kr}}} + 1} \right) T_{s,i+1} \\ & - \frac{kt \sqrt{\frac{h_f+h_m}{kt}}}{\sinh \left(c \sqrt{\frac{h_f+h_m}{kt}} \right)} T_{s,i+2} = \frac{1}{2} krt \tanh \left(\frac{b}{2} \sqrt{\frac{2h_m}{kr}} \right) (T_{f,i} + T_{f,i+1}) \sqrt{\frac{2h_m}{kr}} \\ & + \sqrt{\frac{kt}{h_f+h_m}} \tanh \left(\frac{c}{2} \sqrt{\frac{h_f+h_m}{kt}} \right) [2T_{f,n+1}h_f + (T_{f,i} + T_{f,i+1})h_m] \end{aligned} \quad (45)$$

where $i = 1, 2, 3, \dots, n-1$. Eq. (45) was a linear equation system with $n + 1$ unknown temperatures, e.g., $T_{s,i}$, $T_{s,i+1}$, $T_{s,i+2}$, but there were only $n-1$ equations. In order to enclose the equations, two additional heat flux equilibrium equations were written for the bottom and top substrates, respectively:

$$Q_{o,1} + Q_{sb,1} + Q_{sb,2} = q_1 \left(t + \frac{a+b}{2} \right) \quad (46)$$

$$-Q_{e,n} + Q_{st,1} + Q_{st,2} = q_2 \left(t + \frac{a+b}{2} \right) \quad (47)$$

Substituting Eqs.(4), (19), (26) into Eq.(46) and Eqs. (5), (33), (40) into Eq.(47), we had:

$$\begin{aligned} & k \left[t \coth \left(c \sqrt{\frac{h_f+h_m}{kt}} \right) \sqrt{\frac{h_f+h_m}{kt}} + t_s \left(\tanh \left(\frac{a}{2} \sqrt{\frac{h_f}{kt_s}} \right) \sqrt{\frac{h_f}{kt_s}} + \tanh \left(\frac{b}{2} \sqrt{\frac{h_m}{kt_s}} \right) \sqrt{\frac{h_m}{kt_s}} \right) \right] T_{s,1} \\ & - \frac{kt \sqrt{\frac{h_f+h_m}{kt}}}{\sinh \left(c \sqrt{\frac{h_f+h_m}{kt}} \right)} T_{s,2} = \frac{q_1(a+b+2t)}{2} + T_{f,n+1} kt_s \tanh \left(\frac{a}{2} \sqrt{\frac{h_f}{kt_s}} \right) \sqrt{\frac{h_f}{kt_s}} \\ & + T_{f,1} kt_s \tanh \left(\frac{b}{2} \sqrt{\frac{h_m}{kt_s}} \right) \sqrt{\frac{h_m}{kt_s}} + \frac{kt \tanh \left(\frac{c}{2} \sqrt{\frac{h_f+h_m}{kt}} \right) (T_{f,n+1}h_f + T_{f,1}h_m) \sqrt{\frac{h_f+h_m}{kt}}}{h_f+h_m} \end{aligned} \quad (48)$$

$$\begin{aligned} & k \left[t \coth \left(c \sqrt{\frac{h_f+h_m}{kt}} \right) \sqrt{\frac{h_f+h_m}{kt}} + t_s \left(\tanh \left(\frac{a}{2} \sqrt{\frac{h_f}{kt_s}} \right) \sqrt{\frac{h_f}{kt_s}} + \tanh \left(\frac{b}{2} \sqrt{\frac{h_m}{kt_s}} \right) \sqrt{\frac{h_m}{kt_s}} \right) \right] T_{s,n+1} \\ & - \frac{kt \sqrt{\frac{h_f+h_m}{kt}}}{\sinh \left(c \sqrt{\frac{h_f+h_m}{kt}} \right)} T_{s,n} = T_{f,n+1} kt_s \tanh \left(\frac{a}{2} \sqrt{\frac{h_f}{kt_s}} \right) \sqrt{\frac{h_f}{kt_s}} + T_{f,n} kt_s \tanh \left(\frac{b}{2} \sqrt{\frac{h_m}{kt_s}} \right) \sqrt{\frac{h_m}{kt_s}} \\ & + \frac{kt \tanh \left(\frac{c}{2} \sqrt{\frac{h_f+h_m}{kt}} \right) (T_{f,n+1}h_f + T_{f,n}h_m) \sqrt{\frac{h_f+h_m}{kt}}}{h_f+h_m} + \frac{q_2(a+b+2t)}{2} \end{aligned} \quad (49)$$

Eqs. (45), (48), (49) constituted a system of linear equations about node temperature $T_{s,i}$ ($i = 1, 2, 3, \dots, n + 1$):

$$\begin{bmatrix} \beta_1 & \beta_2 & \cdot & \cdot & \cdot & \cdot & \cdot \\ \beta_2 & \beta_3 & \beta_2 & \cdot & \cdot & \cdot & \cdot \\ \cdot & \beta_2 & \beta_3 & \beta_2 & \cdot & \cdot & \cdot \\ \cdot & \cdot & \cdot & \cdot & \cdot & \cdot & \cdot \\ \cdot & \cdot & \cdot & \beta_2 & \beta_3 & \beta_2 & \cdot \\ \cdot & \cdot & \cdot & \cdot & \beta_2 & \beta_3 & \beta_2 \\ \cdot & \cdot & \cdot & \cdot & \cdot & \beta_2 & \beta_1 \end{bmatrix} \begin{bmatrix} T_{s,1} \\ T_{s,2} \\ T_{s,3} \\ \cdot \\ T_{s,n-1} \\ T_{s,n} \\ T_{s,n+1} \end{bmatrix} = \begin{bmatrix} \gamma_1 \\ \gamma_2 \\ \gamma_3 \\ \cdot \\ \gamma_{n-1} \\ \gamma_n \\ \gamma_{n+1} \end{bmatrix} \quad (50)$$

where,

$$\begin{aligned} \beta_1 & = k \left[t \coth \left(c \sqrt{\frac{h_f+h_m}{kt}} \right) \sqrt{\frac{h_f+h_m}{kt}} + t_s \left(\tanh \left(\frac{a}{2} \sqrt{\frac{h_f}{kt_s}} \right) \sqrt{\frac{h_f}{kt_s}} \right. \right. \\ & \left. \left. + \tanh \left(\frac{b}{2} \sqrt{\frac{h_m}{kt_s}} \right) \sqrt{\frac{h_m}{kt_s}} \right) \right] \end{aligned} \quad (51)$$

$$\beta_2 = -\frac{kt\sqrt{\frac{h_f+h_m}{kt}}}{\sinh\left(c\sqrt{\frac{h_f+h_m}{kt}}\right)} \quad (52)$$

$$\beta_3 = 2kt\coth\left(c\sqrt{\frac{h_f+h_m}{kt}}\right)\sqrt{\frac{h_f+h_m}{kt}} + \frac{kr\left(e^{b\sqrt{\frac{2h_m}{kr}}}-1\right)\sqrt{\frac{2h_m}{kr}}}{e^{b\sqrt{\frac{2h_m}{kr}}}+1} \quad (53)$$

$$\begin{aligned} \gamma_1 = & \frac{q_1(a+b+2t)}{2} + T_{f,n+1}kt_s \tanh\left(\frac{a}{2}\sqrt{\frac{h_f}{kt_s}}\right)\sqrt{\frac{h_f}{kt_s}} + T_{f,1}kt_s \tanh\left(\frac{b}{2}\sqrt{\frac{h_m}{kt_s}}\right)\sqrt{\frac{h_m}{kt_s}} \\ & + \frac{kt \tanh\left(\frac{c}{2}\sqrt{\frac{h_f+h_m}{kt}}\right)(T_{f,n+1}h_f+T_{f,1}h_m)\sqrt{\frac{h_f+h_m}{kt}}}{h_f+h_m} \end{aligned} \quad (54)$$

$$\begin{aligned} \gamma_{n+1} = & \frac{q_2(a+b+2t)}{2} + T_{f,n+1}kt_s \tanh\left(\frac{a}{2}\sqrt{\frac{h_f}{kt_s}}\right)\sqrt{\frac{h_f}{kt_s}} + T_{f,n}kt_s \tanh\left(\frac{b}{2}\sqrt{\frac{h_m}{kt_s}}\right)\sqrt{\frac{h_m}{kt_s}} \\ & + \frac{kt \tanh\left(\frac{c}{2}\sqrt{\frac{h_f+h_m}{kt}}\right)(T_{f,n+1}h_f+T_{f,n}h_m)\sqrt{\frac{h_f+h_m}{kt}}}{h_f+h_m} \end{aligned} \quad (55)$$

$$\begin{aligned} \gamma_{i+1} = & \frac{1}{2}kr \tanh\left(\frac{b}{2}\sqrt{\frac{2h_m}{kr}}\right)(T_{f,i}+T_{f,i+1})\sqrt{\frac{2h_m}{kr}} \\ & + \sqrt{\frac{kt}{h_f+h_m}} \tanh\left(\frac{c}{2}\sqrt{\frac{h_f+h_m}{kt}}\right)[2T_{f,n+1}h_f+(T_{f,i}+T_{f,i+1})h_m] \end{aligned} \quad (56)$$

$i = 1, 2, 3 \dots n - 1$

As the coefficient matrix in Eq.(50) was tridiagonal, direct inversion of the matrix would lead to poor efficiency. Instead, a chasing algorithm was selected to solve the tridiagonal equations [42]. Finally, the function expression (φ_i) of node temperature ($T_{s,i}$) was obtained as a function of fluid temperatures ($T_{f,i}$), as:

$$\begin{bmatrix} T_{s,1} \\ T_{s,2} \\ \dots \\ T_{s,i} \\ \dots \\ T_{s,n} \\ T_{s,n+1} \end{bmatrix} = \begin{bmatrix} \varphi_1(T_{f,1}, T_{f,2} \dots T_{f,n+1}) \\ \varphi_2(T_{f,1}, T_{f,2} \dots T_{f,n+1}) \\ \dots \\ \varphi_i(T_{f,1}, T_{f,2} \dots T_{f,n+1}) \\ \dots \\ \varphi_n(T_{f,1}, T_{f,2} \dots T_{f,n+1}) \\ \varphi_{n+1}(T_{f,1}, T_{f,2} \dots T_{f,n+1}) \end{bmatrix} \quad (57)$$

where φ_i ($i = 1, 2, 3, \dots, n + 1$) was obtained by solving Eq.(50).

2.2. Temperature of fluid along flow direction

As indicated by Eq.(57), in the xy plane perpendicular to flow, the node temperature ($T_{s,i}$) only depended on fluid temperature ($T_{f,i}$) at given z -coordinate. Before the solid temperatures ($T_{s,i}$) at each z plane could be solved, one should first obtain fluid temperature distribution in each individual duct ($T_{f,i}$) along flow direction.

2.2.1. Temperature of fluid in large ducts

In order to solve fluid temperature distribution along flow direction, the heat transfer process of fluid in a large duct was analyzed. At given xy plane, the fluid in the large duct was heated up by three sources: convective heat transfer from the vertical struts, from the top substrate, and from the bottom substrate, i.e., $\Sigma Q_{i,f}$, $Q_{sb,2}$ and $Q_{st,2}$. Note that $Q_{sb,2}$ and $Q_{st,2}$ could be obtained by substituting Eq.(57) into Eqs.(26) and (40), respectively.

Heat transfer from vertical struts between node i to $i + 1$ to the fluid in the large duct ($Q_{i,f}$) was:

$$\begin{aligned} Q_{i,f} = & h_f \int_0^c (T - T_{f,n+1}) dy \\ = & h_f \left(\frac{C_{i,1}}{\lambda_1} (e^{\lambda_1 c} - 1) + \frac{C_{i,2}}{\lambda_2} (e^{\lambda_2 c} - 1) + \frac{h_m}{h_f + h_m} (T_{f,i} - T_{f,n+1}) c \right) \end{aligned} \quad (58)$$

where $i = 1, 2, 3, \dots, n$. Total heat dissipation from n vertical struts to fluid in the large duct was $\Sigma Q_{i,f}$.

Temperature rise of fluid in the large duct along streamwise direction was due to heat input from the bottom and top substrates as well as from the vertical struts. Conservation of energy dictated:

$$\rho u_f \frac{aH}{2} c_p \frac{\partial T_{f,n+1}}{\partial z} = Q_{sb,2} + Q_{st,2} + \sum_{i=1}^n Q_{i,f} \quad (59)$$

where u_f is the average velocity of fluid flow in the large duct.

2.2.2. Temperature of fluid in small ducts

Similarly, at given z plane perpendicular to the flow direction, the fluid in each small duct was heated up by three heat sources: the convective heat transfer from vertical strut (between node i and $i + 1$), from horizontal struts at node i and that at node $i + 1$, denoted by $Q_{i,mv}$, $Q_{i,mhu}$ and $Q_{i,mhd}$ respectively.

Heat dissipation from vertical strut between node i and $i + 1$ to fluid in small duct i ($Q_{i,mv}$) satisfied:

$$\begin{aligned} Q_{i,mv} = & h_m \int_0^c (T - T_{f,i}) dy \\ = & h_m \left(\frac{C_{i,1}}{\lambda_1} (e^{\lambda_1 c} - 1) + \frac{C_{i,2}}{\lambda_2} (e^{\lambda_2 c} - 1) + \frac{h_f}{h_f + h_m} (T_{f,n+1} - T_{f,i}) c \right) \end{aligned} \quad (60)$$

where $i = 1, 2, 3, \dots, n$ represents each small duct from bottom to top.

Heat dissipation from horizontal strut at node i to fluid in small duct i ($Q_{i,mhu}$) satisfied:

$$\begin{aligned} Q_{i,mhu} = & h_m \int_0^{\frac{b}{2}} (T - T_{f,i}) dx \\ = & h_m \left(\frac{D_{i-1,1}}{\mu_1} (e^{\mu_1 \frac{b}{2}} - 1) + \frac{D_{i-1,2}}{\mu_2} (e^{\mu_2 \frac{b}{2}} - 1) + \left(\frac{T_{f,i-1} - T_{f,i}}{2} \right) \frac{b}{2} \right) \end{aligned} \quad (61)$$

where $i = 2, 3, \dots, n$ denotes each horizontal strut from bottom to the top. However, for the small duct nearby the bottom substrate, heat transfer from bottom substrate to fluid was separately determined, as:

$$Q_{1,mhu} = h_m \int_0^{\frac{b}{2}} (T - T_{f,1}) dx = Q_{sb,1} \quad (62)$$

Similarly, heat dissipation from horizontal strut at node $i + 1$ to fluid in small duct i ($Q_{i,mhd}$) satisfied:

$$\begin{aligned} Q_{i,mhd} = & h_m \int_0^{\frac{b}{2}} (T - T_{f,i}) dx \\ = & h_m \left(\frac{D_{i,1}}{\mu_1} (e^{\mu_1 \frac{b}{2}} - 1) + \frac{D_{i,2}}{\mu_2} (e^{\mu_2 \frac{b}{2}} - 1) + \left(\frac{T_{f,i+1} - T_{f,i}}{2} \right) \frac{b}{2} \right) \end{aligned} \quad (63)$$

where $i = 1, 2, 3, \dots, n-1$. For the small duct nearby the top substrate, heat transfer from top substrate to fluid was separately calculated as:

$$Q_{n,mhd} = h_m \int_0^{\frac{b}{2}} (T - T_{f,n}) dx = Q_{st,1} \quad (64)$$

As the rise of fluid temperature in the small duct i was caused by the heat sources of $Q_{i,mv}$, $Q_{i,mhu}$ and $Q_{i,mhd}$, conservation of energy was written as:

$$\rho u_m \frac{bc}{2} c_p \frac{\partial T_{f,i}}{\partial z} = Q_{i,mv} + Q_{i,mhu} + Q_{i,mhd} \quad (65)$$

where u_m is the velocity in small ducts.

2.2.3. Solution of fluid temperatures

Substitution of Eq.(57) into Eqs. (59), (65) yielded a first order system of linear ordinary differential equations about $T_{f,i}$, as:

$$\frac{\partial}{\partial z} \begin{bmatrix} T_{f,1} \\ T_{f,2} \\ \dots \\ T_{f,n} \\ T_{f,n+1} \end{bmatrix} = \begin{bmatrix} G_{1,1} & G_{1,2} & \dots & G_{1,n} & G_{1,n+1} \\ G_{2,1} & G_{2,2} & \dots & G_{2,n} & G_{2,n+1} \\ \dots & \dots & \dots & \dots & \dots \\ G_{n,1} & G_{n,2} & \dots & G_{n,n} & G_{n,n+1} \\ G_{n+1,1} & G_{n+1,2} & \dots & G_{n+1,n} & G_{n+1,n+1} \end{bmatrix} \begin{bmatrix} T_{f,1} \\ T_{f,2} \\ \dots \\ T_{f,n} \\ T_{f,n+1} \end{bmatrix} + \begin{bmatrix} W_1 \\ W_2 \\ \dots \\ W_n \\ W_{n+1} \end{bmatrix} \quad (66)$$

where \mathbf{G} and \mathbf{W} are constant coefficient matrices, both independent of node temperature ($T_{s,i}$) and fluid temperature ($T_{f,i}$) but related to thermal properties and working conditions, e.g., k , k_f , μ , ρ , h_f , h_m , u_f , u_m , a , b , c , H , L , r , t , t_s , q_1 , q_2 , Δp .

2.3. Determination of velocity and interfacial heat transfer coefficient

In order to close the theoretical model, flow velocity and interfacial heat transfer coefficient in the rectangular duct should be determined. This was achieved by employing empirical formula of laminar flow and turbulent flow regions, respectively, as detailed below.

2.3.1. Laminar flow

The friction factor and Nusselt number for fully developed flow in a rectangular pipe with constant heat flux boundary condition were previously correlated as [43]:

$$f \cdot Re = 24\Psi_u \quad (67)$$

$$Nu = 8.235\Psi_h \quad (68)$$

where Re is the Reynolds number, and Ψ_u and Ψ_h are flow shape factors of the duct [9]:

$$f = \frac{\Delta p D}{2\rho u^2 L} \quad (69)$$

$$Re = \frac{\rho u D}{\mu} \quad (70)$$

$$Nu = \frac{h D}{k_f} \quad (71)$$

$$\Psi_u = 1 - 1.3553\alpha + 1.9467\alpha^2 - 1.7012\alpha^3 + 0.9564\alpha^4 - 0.2537\alpha^5 \quad (72)$$

$$\Psi_h = 1 - 2.0421\alpha + 3.0853\alpha^2 - 2.4765\alpha^3 + 1.0578\alpha^4 - 0.1861\alpha^5 \quad (73)$$

Here, D and α are hydraulic diameter and aspect ratio of the duct, respectively. For large ducts, $\alpha = \min[a/H, H/a]$, while for small ducts $\alpha = \min[b/c, c/b]$.

Then Eqs. (67), (68) could be rewritten as follows:

$$u = \frac{\Delta p D^2}{48\mu L(1 - 1.3553\alpha + 1.9467\alpha^2 - 1.7012\alpha^3 + 0.9564\alpha^4 - 0.2537\alpha^5)} \quad (74)$$

$$h = 8.235 \times \frac{k_f}{D} (1 - 2.0421\alpha + 3.0853\alpha^2 - 2.4765\alpha^3 + 1.0578\alpha^4 - 0.1861\alpha^5) \quad (75)$$

2.3.2. Turbulent flow

For non-circular cross-sectional ducts, flow resistance was described by the Karman-Nikuradse relationship [44]:

$$f^{-1/2} = 1.737 \ln[Re f^{1/2}] - 0.396 \quad (76)$$

Heat transfer was described by the Gnielinski formula, which was accurate over a wide range of Reynolds number:

$$Nu = \frac{(f/2)(Re - 10^3)Pr}{1 + 12.7(f/2)^{1/2}(Pr^{2/3} - 1)} \quad (77)$$

Upon substituting Eqs. (69), (70), (71) into Eqs. (76), (77), flow velocity and heat transfer coefficient were determined as:

$$u = \frac{1.737 \ln(2^{-1/2} \Delta p^{1/2} \rho^{1/2} D^{3/2} \mu^{-1} L^{-1/2}) - 0.396}{2^{1/2} \Delta p^{-1/2} \rho^{1/2} L^{1/2} D^{-1/2}} \quad (78)$$

$$h = \frac{\mu c_p}{D} \frac{(f/2)(Re - 10^3)}{1 + 12.7(f/2)^{1/2}((\mu c_p/k_f)^{2/3} - 1)} \quad (79)$$

2.4. Parameters definition

The overall heat transfer coefficient of the hierarchical corrugated sandwich panel was defined as:

$$h_w = \frac{q_{ave}}{T_{s,ave} - T_{f,ave}} \quad (80)$$

where q_{ave} is the constant heat flux imposed to the top and bottom substrates, and $T_{s,ave}$ is the area weighted average temperature of solid at any xy plane in fully developed region:

$$T_{s,ave} = \frac{1}{S} \int T dS = \frac{1}{S} \left(\sum_{i=1}^n \int t T dy + \sum_{i=1}^{n-1} \int r T dx + \int t_s T dx \right) \quad (81)$$

The three items in brackets are the area weighted average temperature of the vertical struts, horizontal struts and substrates, respectively, which could be determined from the known temperature distributions of each solid components. $T_{f,ave}$ is the bulk temperature of fluid at the corresponding xy plane in fully developed region:

$$T_{f,ave} = \frac{1}{uS} \int T u dS = \frac{1}{nu_m bc + u_f aH} \left(u_m bc \sum_{i=1}^n T_{f,i} + u_f aHT_{f,n+1} \right) \quad (82)$$

Finally, the overall Reynolds number, Nusselt number and friction factor of the hierarchical corrugated sandwich panel were defined based on the height of the panel, as:

$$Re_H = \frac{\rho u_w H}{\mu} \quad (83)$$

$$Nu_H = \frac{h_w H}{k_f} \quad (84)$$

$$f_H = \frac{\Delta p H}{2\rho u_w^2 L} \quad (85)$$

3. Numerical simulation

In this section, a numerical model for predicting the convective heat transfer efficiency of the proposed hierarchical corrugated sandwich panel was established.

3.1. Computational domain, governing equations and boundary conditions

Fig. 2(b) presents the computational domain and mesh used for modelling forced convection heat transfer in the hierarchical corrugated sandwich. Due to symmetry of geometry and boundary conditions, only a unit cell was included in the numerical simulation to save computational time. Geometric parameters selected for the case study were listed in Table 1. Thermal properties of the hierarchical structure (made of aluminum) and the cooling fluid (water) were given in Table 2. Both the top and bottom substrates of the sandwich were subjected to a constant heat flux of 10000 W/m². Inlet temperature of the cooling water was fixed at 300 K, while its mean velocity was varied over a wide range and the corresponding Reynolds number changed from 100 to 20000, ranging from laminar, transition to turbulent flow regions. Therefore, both the laminar model and the $k - \epsilon$ turbulence model were tested in the numerical simulation for both laminar and full turbulent flows, respectively. Other assumptions made included:

Table 1
Geometric parameters of the hierarchical structure selected for numerical simulation.

| Height of sandwich panel H (mm) | Length of sandwich panels L (mm) | Width of large ducts a (mm) | Width of small ducts b (mm) | Thickness of vertical strut t (mm) | Thickness of horizontal struts (mm) | Thickness of substrate t_s (mm) | Number of small ducts n |
|-----------------------------------|------------------------------------|-------------------------------|-------------------------------|--------------------------------------|-------------------------------------|-----------------------------------|---------------------------|
| 10 | 3000 | 6 | 6 | 1 | 0.5 | 1 | 2 |

Table 2
Thermal properties of aluminum and water used in numerical simulation.

| Materials | Density ρ (kg/m ³) | Specific heat c_p (J/(kg·K)) | Dynamic viscosity μ (Pa·s) | Thermal conductivity k (W/(mK)) |
|-----------|-------------------------------------|--------------------------------|--------------------------------|-----------------------------------|
| Water | 998.2 | 4182 | 1.003×10^{-3} | 0.6 |
| Aluminum | 2700 | 880 | – | 202 |

- (1) The flow was three-dimensional, incompressible and steady with no viscous dissipation;
- (2) Thermal properties of fluid and solid were constant.

Based on the above assumptions, governing equations of the numerical model are [45]:

Continuity equation:

$$\frac{\partial u_i}{\partial x_j} = 0 \quad (86)$$

Momentum equations:

$$\frac{\partial}{\partial x_j} (\rho u_i u_j) = -\frac{\partial p}{\partial x_i} + \frac{\partial}{\partial x_j} \left(\mu \frac{\partial u_i}{\partial x_j} - \rho \overline{u_i u_j'} \right) \quad (i = 1, 2, 3) \quad (87)$$

Energy equation:

$$\frac{\partial}{\partial x_j} (\rho u_j T) = \frac{\partial}{\partial x_j} \left(\frac{k}{c_p} \frac{\partial T}{\partial x_j} - \rho \overline{u_j T'} \right) \quad (88)$$

where ρ , c_p , μ and k are the density, specific heat, dynamic viscosity and thermal conductivity, respectively.

The Reynolds-averaging equations were employed to deal with turbulence, where $\rho \overline{u_i u_j'}$ was the Reynolds stress generated by instantaneous pulsating flow, and $\rho \overline{u_j T'}$ was the additional term of turbulence pulsation of temperature. The Reynolds stress was related to the average velocity gradient using vortex viscosity coefficient according to the Boussinesq hypothesis, as:

$$-\rho \overline{u_i u_j'} = \tau_{ij} = \mu_t \left(2S_{ij} - \frac{2}{3} \frac{\partial u_i}{\partial x_i} \delta_{ij} \right) - \frac{2}{3} \rho k \delta_{ij} \quad (89)$$

where S_{ij} was the strain rate tensor satisfying:

$$S_{ij} = \frac{1}{2} \left(\frac{\partial u_i}{\partial x_j} + \frac{\partial u_j}{\partial x_i} \right) \quad (90)$$

The temperature transmitted by turbulence pulsation was related to the time-averaging parameters via:

$$-\rho \overline{u_j T'} = \Gamma_t \frac{\partial T}{\partial x_j} \quad (91)$$

In the above equations, μ_t is the turbulent viscous coefficient and Γ_t is the turbulent diffusion coefficient.

The standard k - ϵ turbulent model was chosen to evaluate the turbulent viscous coefficient, as:

Turbulent kinetic energy equation:

$$\rho \frac{\partial k}{\partial t} + \rho u_j \frac{\partial k}{\partial x_j} = \frac{\partial}{\partial x_j} \left[\left(\mu + \frac{\mu_t}{\sigma_k} \right) \frac{\partial k}{\partial x_j} \right] + \mu_t \frac{\partial u_i}{\partial x_j} \left(\frac{\partial u_i}{\partial x_j} + \frac{\partial u_j}{\partial x_i} \right) - \rho \epsilon \quad (92)$$

Turbulence dissipation equation:

$$\rho \mu_k \frac{\partial \epsilon}{\partial x_k} = \frac{\partial}{\partial x_j} \left[\left(\mu + \frac{\mu_t}{\sigma_\epsilon} \right) \frac{\partial \epsilon}{\partial x_k} \right] + \frac{c_1 \epsilon}{k} \mu_t \frac{\partial u_i}{\partial x_j} \left(\frac{\partial u_i}{\partial x_j} + \frac{\partial u_j}{\partial x_i} \right) - c_2 \rho \frac{\epsilon^2}{k} \quad (93)$$

The turbulence viscosity and turbulent diffusion coefficient could be evaluated as:

$$\mu_t = \rho c_\mu \frac{k^2}{\epsilon} \quad (94)$$

$$\Gamma_t = \frac{\mu}{Pr} + \frac{\mu_t}{\sigma_t} \quad (95)$$

where σ_t is the turbulent Prantl number related to the temperature field: μ/Pr is caused by molecular diffusion, while μ_t/σ_t is due to turbulent fluctuation. The model coefficients and constants selected in the present study were: $c_1 = 1.44$, $c_2 = 1.92$, $c_\mu = 0.09$, $\sigma_k = 1.0$, $\sigma_\epsilon = 1.3$, $\sigma_t = 0.95$.

Pressure boundary conditions were applied to the inlet and outlet of the computational domain, respectively. The top substrate was heated by uniform heat flux. Symmetry boundary condition was applied to the two sides and the bottom surface of the computational domain. The remaining solid walls were thermally adiabatic. The above boundary conditions can be mathematically described as [9]:

Inlet:

$$p = \Delta p, T_c = 300K \quad (96)$$

Outlet:

$$p = 0, \frac{\partial T}{\partial z} = 0 \quad (97)$$

Two sides and bottom:

$$\frac{\partial u}{\partial n} = \frac{\partial v}{\partial n} = \frac{\partial w}{\partial n} = \frac{\partial T}{\partial n} = 0 \quad (98)$$

Top:

$$q = -k \frac{\partial T}{\partial n} \quad (99)$$

Solid walls at inlet/outlet:

$$u = v = w = 0, q = 0 \quad (100)$$

where Δp is the applied pressure drop across the length of sandwich panel, and q is the uniform heat flux applied to the substrates.

3.2. Numerical methods

A multi-block structured mesh incorporating fully hexahedral elements was generated by Gambit 2.4.6 in all fluid and solid domains [9]. A commercial CFD code (ANSYS Fluent 14.5) was used to solve the current problem. The SIMPLE algorithm was applied to couple the pressure and velocity for numerical analysis. A second-order upwind scheme was applied to discretize the convective terms in the governing equations. The iterative convergence criterion was chosen as 10^{-5} for momentum equation and 10^{-6} for energy equation [46] which were verified to be small enough to ensure the numerical results independent of the selected values. The grid dependency was also

checked with the number of elements increasing from 200 thousand to 2 million, and the results showed no difference.

4. Results and discussion

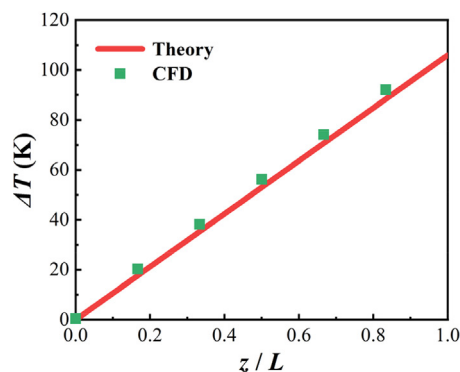
4.1. Theoretical model verification

Firstly, the theoretical model was verified under laminar flow condition by comparing the predicted fluid and solid temperature distributions along the z -coordinate against CFD results, as shown in Fig. 3. In the case study, heat flux on the top and bottom substrates was fixed at $q_1 = q_2 = 200 \text{ W/m}^2$, and pressure drop was set as $\Delta p = 200 \text{ Pa}$. The corresponding Reynolds number of large and small ducts were 647 and 368, respectively. Both the theoretical and CFD predictions showed that the temperatures of fluid and solid in the hierarchical corrugated sandwich increase linearly along streamwise direction, with the relative error between the two approaches $< 5\%$. Actually, although the heat transfer performance of a hierarchical sandwich is determined by both solid heat conduction and fluid convection, the fluid convective effect is significantly stronger than that of heat conduction. It is therefore reasonable to ignore heat conduction along streamwise direction (*i.e.*, z direction) for theoretical modeling.

Next, after validating the theoretical model in laminar flow, the model was extended to turbulent flow by replacing the empirical correlations, as discussed in the next section.

4.2. Flow transition from laminar to turbulence within the sandwich panel

Flow characteristics within the hierarchical corrugated sandwich panel would change with varying Reynolds number, from laminar, transition to turbulent flow. Due to its non-homogeneous duct size, at moderate Reynolds numbers, flow in small ducts may be laminar but may change to turbulent in large ducts. However, at smaller and larger Reynolds numbers, flow in the whole sandwich panel would be purely laminar and turbulent, respectively. To identify the flow stage, a typical hierarchical corrugated sandwich with the geometrical parameters of $H = 10 \text{ mm}$, $t = 1 \text{ mm}$, $r = 1 \text{ mm}$, $t_s = 1 \text{ mm}$, $L = 3000 \text{ mm}$, and $n = 2$ was investigated in the full range of Reynolds number, from laminar to turbulent flow. Corresponding Nu - Re and f - Re curves obtained from both the theory and CFD simulation were displayed in Fig. 4(a) and (b), respectively. For CFD simulations, both the laminar and turbulent models were examined in the full range of Reynolds number. The k - ϵ turbulence model with standard wall function was used in turbulence simulation, where the non-dimensional distance from the first grid to the wall (y^+) was within $30 \sim 50$ [45]. For theoretical model prediction, laminar or turbulent correlation was applied depending upon the actual Reynolds number in each individual duct.



According to Fig. 4, flow state in the sandwich could be divided into three regions according to the Reynolds number, as:

- (1) In the laminar flow region ($Re_H < 2300$), flow in both large ducts ($Re_f < 2300$) and small ducts ($Re_m < 770$) was laminar. Our theory and CFD model both revealed that the friction coefficient decreased rapidly, while the Nusselt number remained almost constant as increasing the Reynolds number. The CFD laminar model was more consistent with the theory relative to the turbulence model.
- (2) In the transition flow region ($2300 < Re_H < 6000$), flow states in large ducts ($2300 < Re_f < 5100$) and small ducts ($770 < Re_m < 2600$) were not consistent. Flow in the small ducts was laminar whereas in the large ducts it was unstable and chaotic due to the disturbance. In this flow stage, neither the steady-state laminar CFD model nor the $k - \epsilon$ turbulence model agreed with the theoretical predictions.
- (3) In the vigorous turbulent flow region ($Re_H > 6000$), the Reynolds number in large ducts ($Re_f > 5100$) and small ducts ($Re_m > 2600$) guaranteed complete turbulent flow in the whole sandwich panel. The friction coefficient tended to be constant after a sharp drop in the laminar and transition regions. The $k - \epsilon$ turbulent model predicted this trend accurately and matched the theoretical predictions better than the laminar model, for both hydrodynamics and heat transfer.

The theoretical model had been verified both in laminar and turbulent flow regions, and hence could be applied in the full flow range for optimal cooling design.

4.3. Parametrical studies

4.3.1. Effects of width ratio of large to small ducts on heat transfer

With the width of large ducts fixed, increasing the width of small ducts would enlarge the total heat dissipation surface area of the sandwich, but meanwhile increase the flow resistance. Therefore, there may exist an optimal ratio of width between the large and small ducts at which the heat transfer of the sandwich is maximized at given pressure drop.

Fig. 5 plotted the overall Nusselt number of the sandwich as a function of the width ratio (a/b) of large to small ducts in laminar flow. Upon considering the limits of manufacturing capacity, the width ratio was varied in the range of $0.1 \sim 3$. The results showed that at small width of large ducts, *e.g.*, $a < 2 \text{ mm}$, heat transfer first increased and then decreased as increasing the width ratio of the large to small ducts, and there existed an optimal width ratio. Nevertheless, if the width of large ducts was larger, *e.g.*, $a > 2 \text{ mm}$, heat transfer decreased monotonously as increasing the width ratio within the investigated

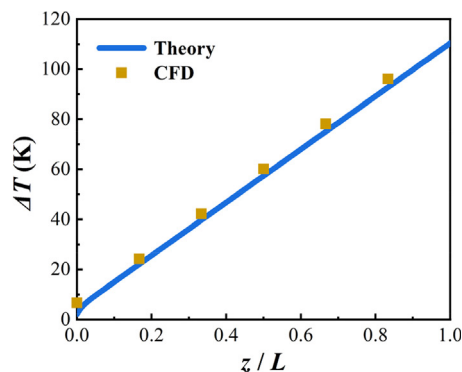


Fig. 3. Comparison of theoretically and numerically predicted temperature distributions of hierarchical corrugated sandwich panel along streamwise direction: (a) cross-sectional average temperature of fluid; (b) cross-sectional average temperature of solid ($\Delta p = 200 \text{ Pa}$, $Re = 647$, $q_1 = q_2 = 200 \text{ W/m}^2$).

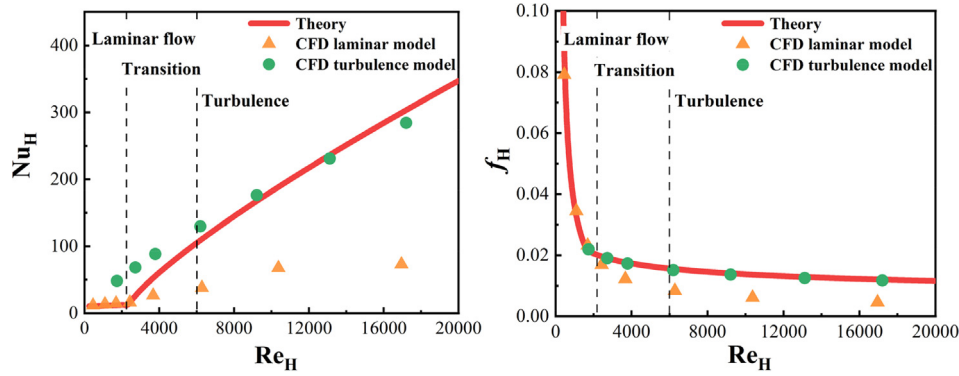


Fig. 4. Comparison of theoretical model predictions and CFD simulation results of (a) heat transfer and (b) friction coefficient for hierarchical corrugated sandwich panel.

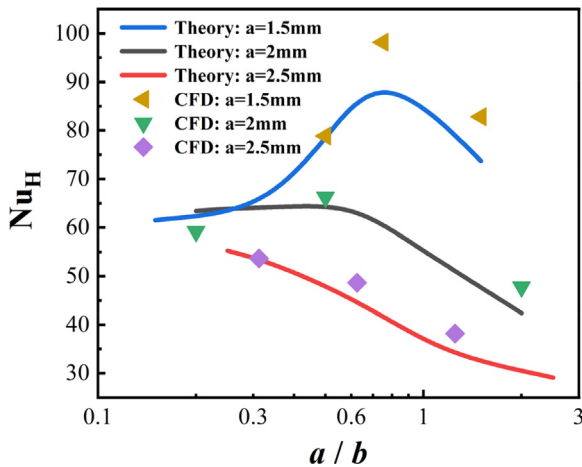


Fig. 5. Influence of width ratio of large to small ducts on heat transfer of hierarchical corrugated sandwich panel under fixed pressure drop in laminar flow ($n = 4$).

range of parameters. It is worth noting that, under laminar flow condition, the heat transfer efficiency of the sandwich is independent of Reynolds number (or pressure drop), thus the optimal width ratio is constant with varying Reynolds number in laminar flow.

Fig. 6(a) plotted the overall Nusselt number as a function of the width ratio of large to small ducts under turbulent flow condition. Similar to the case of laminar flow (Fig. 5), when the width of large ducts was small, e.g., $a < 4$ mm, heat transfer first increased and then

decreased with the increase of width ratio, resulting in an optimal width ratio. However, at larger width of the large ducts, e.g., $a > 4$ mm, heat transfer decreased monotonically as the width ratio was increased. Unlike laminar flow, the Nusselt number in turbulent flow depends on the Reynolds number, so the optimal width ratio would also change with the Reynolds number (or pressure drop). Fig. 6(b) showed that the optimal width ratio increased as the pressure drop (or Reynolds number) was increased. In other words, if the width of large ducts was fixed (e.g., $a = 1.5$ mm) but the pressure drop was increased, the sandwich panel tended to decrease the size of small ducts for optimal heat transfer efficiency.

4.3.2. Effect of the number of small ducts on heat transfer

With all other parameters unchanged, increasing the number of small ducts increases heat dissipation surface area, but meanwhile increases flow resistance. The two competing effects may lead to the presence of an optimal number of small ducts for maximum heat transfer under fixed pressure drop.

Fig. 7 showed the variation of overall Nusselt number with increasing number of small ducts at fixed pressure drop in laminar flow. The heat transfer increased first and then decreased as increasing the number of small ducts if the width ratio (a/b) was < 1 . If the width ratio $a/b \geq 1$ (green line in Fig. 7), the heat transfer decreased monotonically with increasing number of small ducts. In addition, at fixed width ratio, e.g., $a/b = 0.5$, the smaller the duct width, the better the overall heat transfer. On the other hand, at fixed width of large ducts, e.g., $a = 2$ mm, as increasing the width ratio from 0.25 to 0.5 to 1.0, the optimal number of small ducts tended to decrease.

In the turbulent flow region, as shown in Fig. 8(a), the Nusselt number decreased monotonously with increasing number of small ducts

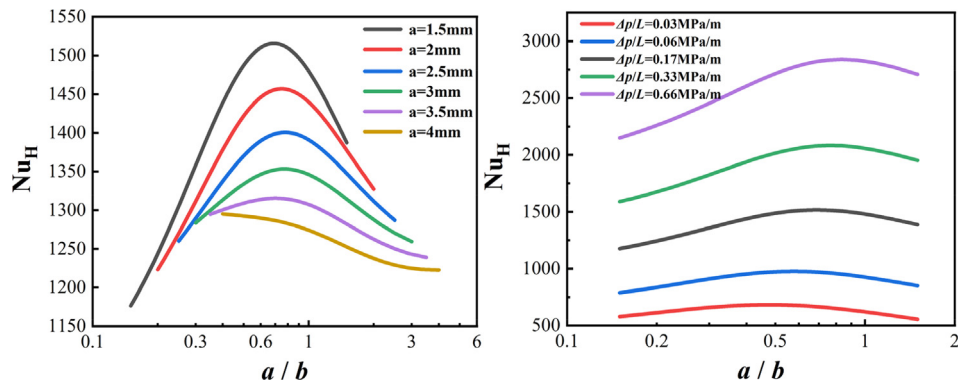


Fig. 6. Influence of width ratio of large to small ducts on heat transfer performance of hierarchical corrugated sandwich panel in turbulent flow condition ($n = 4$) at: (a) fixed pressure drop of $\Delta p/L = 0.167$ MPa/m; (b) fixed width of large duct of $a = 1.5$ mm.

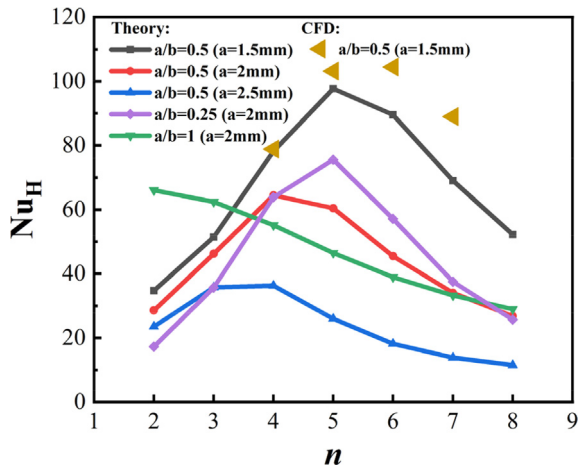


Fig. 7. Effect of the number of small ducts on heat transfer of hierarchical corrugated sandwich under fixed pressure drop in laminar flow.

when the width ratio was large, e.g., $a/b \geq 0.3$. If the width ratio was small, e.g., $a/b = 0.2$, the Nusselt number first slightly increased then decreased as the number of small ducts was increased, consistent with the case of laminar flow; nevertheless, the Nusselt number was not sensitive to the change of the number of small ducts. Fig. 8(b) presented the variation of Nusselt number with the number of small ducts at five different pressure drops (flow velocity or Reynolds number) in turbulent flow. It was found that the optimum number of small ducts tended to increase as flow velocity in the sandwich structure was increased.

5. Optimization of the hierarchical sandwich panel using ant colony algorithm

5.1. Optimization problem description

The previous section showed that the overall heat transfer of hierarchical corrugated sandwich could be enhanced by optimizing a single geometric parameter such as width ratio of small to large ducts, with other parameters fixed. However, it was difficult to find the optimal combination of parameters using traditional methods such as the exhaustive search method. In this section, to maximize the cooling efficiency under given pressure drop, the five independent geometric parameters were simultaneously optimized using the ant colony algorithm.

The optimization problem was defined as below. Inlet temperature of cooling fluid ($T_c = 300$ K) and heat flux imposed on top and bottom

substrates ($q_1 = q_2 = 10000$ W/m²) were all fixed. The objective was to find the maximum Nusselt number (Nu_H) under given pressure drop, while the design variables were the five geometric parameters (a, b, t, r, n). The objective function and the corresponding constraints were:

$$\begin{aligned} \text{Max} \quad & Nu_H = \frac{h_w H}{k_f} \\ \text{s.t.} \quad & 1 \text{ mm} \leq a \leq 10 \text{ mm} \\ & 1 \text{ mm} \leq b \leq 10 \text{ mm} \\ & 0.1 \text{ mm} \leq t \leq 3 \text{ mm} \\ & 0.1 \text{ mm} \leq r \leq 1 \text{ mm} \\ & n = 2, 3, 4 \dots \end{aligned} \tag{101}$$

where the range of geometric parameters were determined according to the limits of manufacturing capacity.

5.2. Optimization methods

In the 1990 s, Dorigo et al. [47] found that when searching for food, ant colony could exchange foraging information by secreting a kind of biological hormone called pheromone to quickly find the target. Based on this phenomenon, a new simulated evolutionary algorithm, i.e., the ant colony algorithm was proposed. As a general stochastic optimization method, the ant colony algorithm is a bionic algorithm which imitates the search mechanism of ants, and has achieved success in solving a series of combinatorial optimization problems, e.g., the famous traveling salesman problem (TSP) [48] the vehicle scheduling problem, the integrated circuit design, the communication network, and the data clustering analysis [49].

However, at present, the application scenarios of ant colony algorithm were mainly restricted to discrete optimization problems: the algorithm was not yet applied to complex continuous optimization problems. This study attempted to employ this intelligent bionic algorithm to solve the optimization problem for bionic engineering structures.

Fig. 9 (a) illustrated the core idea of ant colony algorithm and the process of searching the maximum value of a function. Assume that the function has multiple local peaks. At the beginning, a group of ants are randomly distributed in the entire function domain: some ants are located near the wave crest and some close to the wave trough where the whole system is disordered. Each ant would produce different amount of pheromone before the next movement according to its current position, i.e., the ant at the higher position would produce more pheromone and inversely the ant at the lower position would produce less pheromone. Then the ants at the position with less pheromone have a high probability moving toward the position with more pheromone, while the ants at the position with more pheromone have a high probability exploring around themselves randomly. Finally, all of the ants tend to move toward the position of the highest amount of pher-

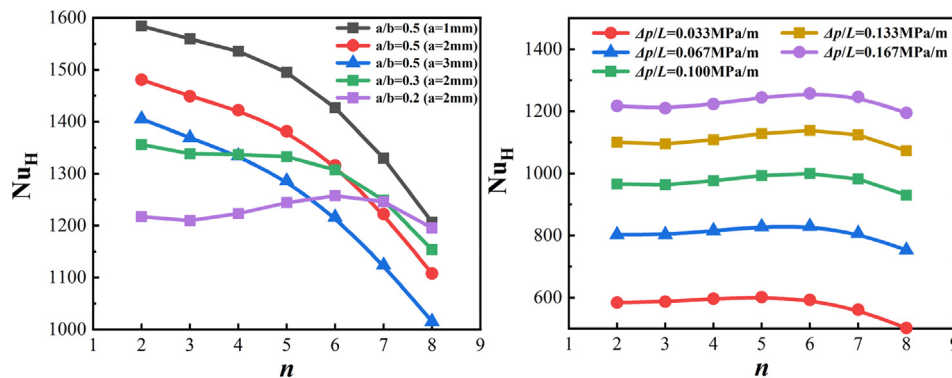


Fig. 8. Influence of the number of small ducts on heat transfer characteristics in turbulent flow at: (a) fixed pressure drop per unit length with $\Delta p/L = 0.167$ MPa/m; (b) fixed large and small ducts width with $a = 2$ mm and $b = 10$ mm, respectively.

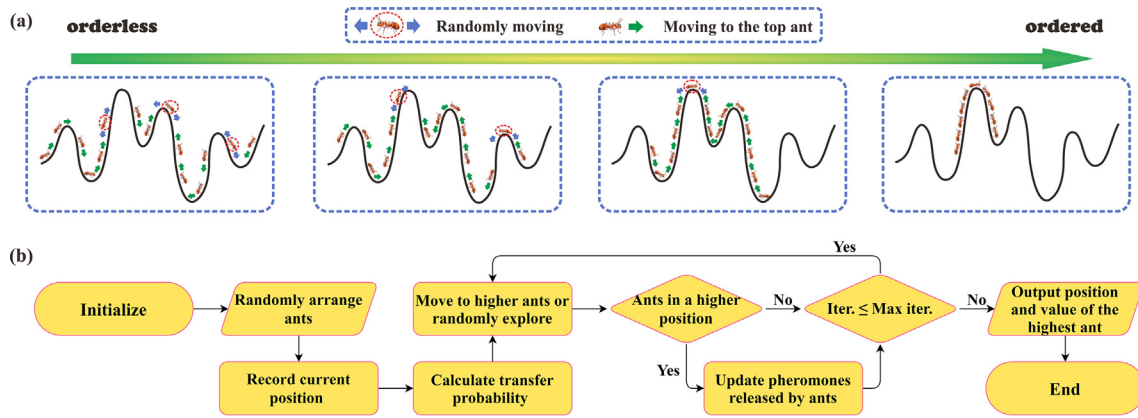


Fig. 9. Ant colony optimization: (a) schematics of searching the maximum value of continuous function; (b) flow chart.

Table 3

Performance comparison between ant colony algorithm and exhaustive search method.

| | Time complexity | Spatial complexity | Nu_H ($\Delta p = 10^5 \text{Pa}$) | Time consumption |
|----------------------|-----------------|--------------------|--|------------------|
| Exhaustive search | $O(n^5)$ | $O(n^5)$ | 771.35 | 162 h |
| Ant colony algorithm | $O(n^2)$ | $O(n^2)$ | 770.07 | 10.3 h |

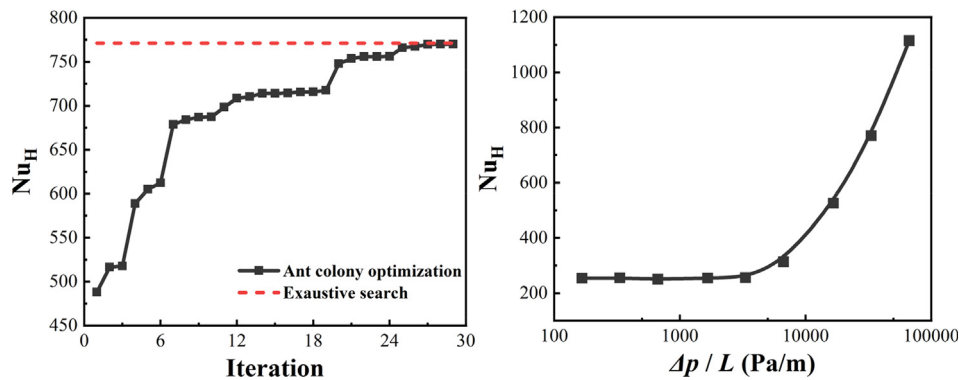


Fig. 10. Optimization results: (a) representative iterative process of ant colony optimization and optimization result of exhaustive search at fixed pressure drop of $\Delta p/L = 3.3 \times 10^4 \text{ Pa/m}$; (b) maximum Nusselt number of hierarchical corrugated sandwich under different pressure drops optimized by ant colony algorithm.

omone. After a limited number of movements, the “pheromones” in the global highest position would attract more and more ants to gather there, *i.e.*, the ants would eventually gather around the maximum value of the function and the whole system becomes ordered.

5.3. Optimization results

The heat transfer optimization of hierarchical corrugated sandwich panels is essentially an optimization problem with 5 variables subjected to constraints. Applying the ant colony algorithm can quickly provide a solution close to the global optimum. In contrast, the exhaustive search method needs 5 layers of loop nesting to search the optimum solution which is time-consuming. In order to compare the two methods, we quantified the spatial/time complexity of the ant colony algorithm and the exhaustive search method, respectively. As shown in Table 3, in terms of spatial and time complexity, the ant colony algorithm was 3 orders of magnitude less than the exhaustive search method, and the time consumption of the former was only 1/16 of the latter.

As shown in Fig. 10(a), the ant colony optimization experienced an iterative process, advancing to the global optimal solution through repeated search. Although the final solution may not be the global

optimal solution, the deviation between the final solution and the global optimal solution was only 0.1%. Upon using the ant colony algorithm, we successfully found the maximum heat transfer efficiency of the proposed hierarchical corrugated sandwich panel and the corresponding optimized geometric parameters at different pressure drops. Fig. 10(b) plotted the maximum Nusselt number as a function of pressure drop. The optimal Nusselt number did not change with pressure drop in laminar flow, consistent with the existing conclusion of duct flow that the Nusselt number exhibits a constant value in laminar flow [44]. Nevertheless, in turbulent flow, the optimal Nusselt number increased significantly with increasing pressure drop, as shown in Fig. 10 (b).

6. Conclusion

The active cooling efficiency of a novel hierarchical corrugated sandwich panel was theoretically and numerically investigated. A theoretical model coupling heat conduction in cell wall and fluid convection in the multi-ducts of the hierarchical porous structure was established, which was validated against CFD simulations from laminar to turbulent flow. Based on the theoretical model, the influence of key geometric parameters such as the large-to-small duct width

ratio and the number of small flow ducts on overall heat transfer was quantified. It was found that there existed optimal width ratio of large to small ducts or optimal number of small ducts if other parameters were fixed. To solve the multivariable optimization problem, the ant colony algorithm was used to find the optimal combination of geometric parameters of the hierarchical corrugated sandwich for maximum heat transfer. It was found that the optimal Nusselt number of the sandwich is constant in laminar flow but increases with increasing flow velocity in turbulent flow.

CRedit authorship contribution statement

Shanyouming Sun: Investigation, Software, Data curation, Validation, Formal analysis, Writing - original draft. **Yinglong Sheng:** Visualization. **Shangsheng Feng:** Conceptualization, Methodology, Writing - review & editing, Funding acquisition. **Tian Jian Lu:** Supervision, Writing - review & editing, Formal analysis, Funding acquisition.

Declaration of Competing Interest

The authors declare that they have no known competing financial interests or personal relationships that could have appeared to influence the work reported in this paper.

Acknowledgements

This work was supported by the National Natural Science Foundation of China (51676156, 11972185 and 12032010), the National "111" Project of China (B06024), the Postdoctoral Science Foundation of China (2016M590942), and the Open Fund of the State Key Laboratory of Mechanics and Control of Mechanical Structures (MCMS-E0219K02, MCMS-I-0219K01).

References

- Jia Z, Yu Y, Hou S, et al. Biomimetic architected materials with improved dynamic performance. *J Mech Phys Solids* 2019;125:178–97.
- Rabiei R, Dastjerdi AK, Mirkhalaf M, et al. Hierarchical structure, mechanical properties and fabrication of biomimetic biomaterials. *Biomimetic Biomater* 2013;67–90.
- Barthelat F. Biomimetics for next generation materials. *Philos Trans R Soc A Math Phys Eng Sci* 1861;2007(365):2907–19.
- Fratzl P. Biomimetic materials research: what can we really learn from nature's structural materials. *J R Soc Interface* 2007;4(15):637–42.
- Liu Z, Meyers MA, Zhang Z, et al. Functional gradients and heterogeneities in biological materials: Design principles, functions, and bioinspired applications. *Prog Mater Sci* 2017;88:467–98.
- Wegst UGK, Bai H, Saiz E, et al. Bioinspired structural materials. *Nat Mater* 2015;14:23–35.
- Valdevit L, Vermaak N, Zok FW, et al. A materials selection protocol for lightweight actively cooled panels. *J Appl Mech* 2008;75(6):061022.
- Mellor AM. *Design of modern combustors*. New York: Academic Press; 1991.
- Sun S, Feng S, Zhang Q, et al. Forced convection in additively manufactured sandwich-walled cylinders with thermo-mechanical multifunctionality. *Int J Heat Mass Transf* 2020;149:119161.
- Zhang Y, Wang J, Wang C, et al. Crashworthiness of bionic fractal hierarchical structures. *Mater Des* 2018;158:147–59.
- Sun Y, Pugno NM. In plane stiffness of multifunctional hierarchical honeycombs with negative Poisson's ratio sub-structures. *Compos Struct* 2013;106:681–9.
- Kooistra GW, Deshpande V, Wadley HNG, et al. Hierarchical corrugated core sandwich panel concepts. *J Appl Mech* 2007;74:259–68.
- Fan HL, Jin FN, Fang DN. Mechanical properties of hierarchical cellular materials. Part I: Analysis. *Compos Sci Technol* 2008;68(15–16):3380–7.
- Sun Y, Pugno NM. In plane stiffness of multifunctional hierarchical honeycombs with negative Poisson's ratio sub-structures. *Compos Struct* 2013;106:681–9.
- Sun FF, Lai CL, Fan HL. In-plane compression behavior and energy absorption of hierarchical triangular lattice structures. *Mater Des* 2016;100:280–90.
- Taylor CM, Smith CW, Miller W, et al. Functional grading in hierarchical honeycombs: Density specific elastic performance. *Compos Struct* 2012;94(8):2296–305.
- Tao Y, Li W, Wei K, et al. Mechanical properties and energy absorption of 3D printed square hierarchical honeycombs under in-plane axial compression. *Compos Part B Eng* 2019;176:107219.
- Wu Q, Gao Y, Wei X, et al. Mechanical properties and failure mechanisms of sandwich panels with ultra-lightweight three-dimensional hierarchical lattice cores. *Int J Solids Struct* 2018;132–133:171–87.
- Wu Q, Vaziri A, Asl ME, et al. Lattice materials with pyramidal hierarchy: Systematic analysis and three dimensional failure mechanism maps. *J Mech Phys Solids* 2019;125:112–44.
- Sun GY, Jiang H, Fang JG, et al. Crashworthiness of vertex based hierarchical honeycombs in out-of-plane impact. *Mater Des* 2016;110:705–19.
- Zhang Y, Lu MH, Wang CH, et al. Out-of-plane crashworthiness of bio-inspired self-similar regular hierarchical honeycombs. *Compos Struct* 2016;144:1–13.
- Hu D, Wang Y, Song B, et al. Energy-absorption characteristics of a bionic honeycomb tubular nested structure inspired by bamboo under axial crushing. *Compos Part B Eng* 2019;162:21–32.
- Yin H, Huang X, Scarpa F, et al. In-plane crashworthiness of bio-inspired hierarchical honeycombs. *Compos Struct* 2018;192:516–27.
- Chen Y, Jia Z, Wang L, et al. Hierarchical honeycomb lattice metamaterials with improved thermal resistance and mechanical properties. *Compos Struct* 2016;152:395–402.
- Xu Z, Buehler MJ. Hierarchical nanostructures are crucial to mitigate ultrasmall thermal point loads. *Nano Lett* 2009;9(5):2065–72.
- Zhu H, Jia Z, Chen Y, et al. Tin anode for sodium-ion batteries using natural wood fiber as a mechanical buffer and electrolyte reservoir. *Nano Lett* 2013;13:3093–100.
- Sutton GP, Biblarz O. *Rocket propulsion elements*. New Jersey: John Wiley & Sons Inc; 2017.
- Song J, Sun B. Coupled numerical simulation of combustion and regenerative cooling in LOX/Methane rocket engines. *Appl Therm Eng* 2016;106:762–73.
- Feng SS, Kim T, Lu TJ. A semi-empirical heat transfer model for forced convection in pin-fin heat sinks subjected to nonuniform heating. *ASME J Heat Transfer* 2010;132:121702.
- Feng SS, Kim T, Lu TJ. Thermomechanical properties of brazed wire-woven bulk kagome cellular metals for multifunctional applications. *J Thermophys Heat Transfer* 2012;26(1):66–74.
- Lu TJ, Valdevit L, Evans AG. Active cooling by metallic sandwich structures with periodic cores. *Prog Mater Sci* 2005;50:789–815.
- Kim T, Hodson HP, Lu TJ. Fluid-flow and endwall heat-transfer characteristics of an ultralight lattice-frame material. *Int J Heat Mass Transf* 2004;47:1129–40.
- Zhao CY. Review on thermal transport in high porosity cellular metal foams with open cells. *Int J Heat Mass Transf* 2012;55:3618–32.
- Zhao CY, Kim T, Lu TJ, et al. Thermal transport in high porosity cellular metal foams. *J Thermophys Heat Transfer* 2004;18(3):309–17.
- Tian J, Lu TJ, Hodson HP, et al. Cross flow heat exchange of textile cellular metal core sandwich panels. *Int J Heat Mass Transf* 2007;50:2521–36.
- Wen T, Tian J, Lu TJ, et al. Forced convection in metallic honeycomb structures. *Int J Heat Mass Transf* 2006;49:3313–24.
- Lu TJ. Heat transfer efficiency of metal honeycombs. *Int J Heat Mass Transf* 1999;42:2031–40.
- Feng S, Li F, Zhang F, et al. Natural convection in metal foam heat sinks with open slots. *Exp Therm Fluid Sci* 2018;91:354–62.
- Lu TJ, Xu F, Wen T. *Thermo-fluid behaviour of periodic cellular metals*. Beijing: Science Press; 2013.
- Zhao CY, Lu TJ. Analysis of microchannel heat sinks for electronics cooling. *Int J Heat Mass Transf* 2002;45:4857–69.
- Liu S, Zhang Y, Liu P. New analytical model for heat transfer efficiency of metallic honeycomb structures. *Int J Heat Mass Transf* 2008;51:6254–8.
- Li W, Ma M. A chasing method for solving cyclic tridiagonal equations. *Sci Technol Rev* 2009;27(14):69–72.
- Shah RK, London AL. *Laminar flow forced convection in ducts: a source book for compact heat exchanger analytical data*. New York: Academic Press; 1978.
- Bejan A. *Convection heat transfer*. New York: John Wiley & Sons Inc.; 1995.
- ANSYS Inc. *ANSYS FLUENT 14.5 User's & Tutorial Guide*. ANSYS Inc., Canonsburg, PA, 2012.
- Feng SS, Sun S, Yan H, et al. Optimum composition of gas mixture in a novel chimney-based led bulb. *Int J Heat Mass Transf* 2017;115:32–42.
- Dorigo M, Caro GD. Ant algorithms for discrete optimization. *Artif Life* 1999;5:137–72.
- Dorigo M, Gambardella LM. Ant colonies for the travelling salesman problem. *BioSystems* 1997;43:73–81.
- Karaboga D, Gorkemli B, Ozturk C, et al. A comprehensive survey: artificial bee colony (ABC) algorithm and applications. *Artif Intell Rev* 2014;42:21–57.